A Cohesive Approach to Thin-Shell Fracture and Fragmentation

Fehmi Cirak[1], Michael Ortiz[2] and Anna Pandolfi[3]

[1]*Center for Advanced Computing Research*
[2]*Graduate Aeronautical Laboratories*
California Institute of Technology
Pasadena, CA 91125, U.S.A.

[3] *Structural Engineering Department*
Politecnico di Milano
20133 Milano, Italy

Abstract

We develop a finite-element method for the simulation of dynamic fracture and fragmentation of thin-shells. The shell is spatially discretized with subdivision shell elements and the fracture along the element edges is modeled with a cohesive law. In order to follow the propagation and branching of cracks, subdivision shell elements are pre-fractured *ab initio* and the crack opening is constrained prior to crack nucleation. This approach allows for shell fracture in an in-plane tearing mode, a shearing mode, or a bending of hinge mode. The good performance of the method is demonstrated through the simulation of petalling failure experiments in aluminum plates.

Keywords: shells, finite elements, subdivision shape functions, cohesive fracture, petalling failure.

1 Introduction

The experimental and analytical investigation of fracture and fragmentation of thin-plates and shells has elicited considerable interest in the past (see, e. g., [13; 14; 27; 32; 33]). The analytic models proposed to date often introduce ad-hoc approximations regarding the likely failure modes and are restricted to a few regular geometries, loading conditions, and constitutive models. By contrast, numerical simulation of fracture and fragmentations of shells and plates has received comparatively less attention. A notable exception is furnished by the finite element analysis of "surface-cracked" plates and shells [12; 15; 24]. In [25], Rice and Levy introduced the concept of a line-spring with stretching and bending resistance for the analytical treatment of plates with a surface crack, and computed its compliance from fracture mechanics and energetic considerations. In the finite element context the line-spring is inserted at the location of the surface-crack in the plate or shell in order to compute quantities relevant for fracture mechanics [24].

In the present work, fracture initiation and propagation is considered as a progressive failure phenomenon in which the separation of the crack flanks is resisted by cohesive tractions. The relationship between the crack opening displacements and the tractions is given by a cohesive model. An appealing feature of the cohesive model is that it provides a complete theory of fracture without presuming a particular bulk material behavior or geometry of the specimen and the extent of the crack growth. In addition, cohesive models are able to overcome several shortcomings of classical fracture mechanics. For example, in fracture mechanics the conditions for crack growth are typically expressed in terms of parameters characterizing the amplitude of near-tip fields. This restricts the scope of the theory, e. g., by requiring that the plastic or process zone be small relative to crack dimensions.

For three-dimensional solids, cohesive laws may conveniently be encoded into cohesive elements in the form of double surfaces (e. g., [4; 17; 18; 19; 20; 21; 22; 23; 30; 35] and references therein). The opening of the cohesive elements is compatible with the deformation of the adjacent volume elements and is subject to a unilateral closure constraint. Cohesive elements may be inserted adaptively upon the attainment of a critical stress condition on the interelement boundary [4; 22; 23]. The insertion of cohesive elements introduces new surfaces into the mesh, which undergoes complex topological transitions as a result. For three-dimensional solids these transitions can be classified exhaustively [22; 23], and appropriate actions may be taken in order to update the representation of the mesh in each case.

Certain aspects of the mechanics of thin-shells greatly compound the integration of cohesive theories of fracture. Thus, within the framework of Kirchhoff-Love theory the strain energy density of thin shells is expressed in terms of the first and second fundamental forms of the shell middle surface. Therefore, a conforming finite element discretization requires smooth shape functions belonging to the Sobolev space H^2. Cirak, Ortiz, and Schröder [5; 6] proposed a new type of discretization based on the concept of subdivision surfaces which delivers smooth H^2 shape functions on unstructured meshes in a particularly natural and efficient way. In addition to several other advantages, an appealing feature of the subdivision elements is that the sole unknowns in the finite element solution are the nodal displacements. However, this comes at a certain cost, namely, that the subdivision shape functions are non-local in the sense that the displacement field within one element depends on the displacements of the nodes attached to the element and the immediately adjacent ring of nodes in the mesh.

The natural extension of the cohesive element concept to shells consists of inserting cohesive

elements at interelement edges, and constraining the opening of the cohesive elements to conform to the deformation of the middle surface of the shell and its normal. This approach allows for fracture in an in-plane or tearing mode, a shearing mode, or a bending of hinge mode. However, within a subdivision-element framework the essential difficulty resides in making the scheme adaptive, in the sense of inserting cohesive elements in an otherwise conforming mesh upon the attainment of some appropriate critical condition. The non-locality of the displacement interpolation renders the tracking of the topological transitions induced by the insertion of cohesive elements unmanageably complex. In order to sidestep this difficulty, we simply fragment *ab initio* all the element edges by duplication of common nodes. In calculations, element conformity prior to fracture is enforced by the addition of a penalty term to the energy. Alternatively, in explicit dynamics calculations conformity is readily enforced by a displacement averaging technique.

The organization of the paper is as follows. In Section 2 we introduce the used thin-shell theory; we describe the kinematics, derive the weak form of the equilibrium equation, and introduce the spatial discretization with subdivision shape functions. The material models for bulk and cohesive surfaces are described in Section 4. In Section 5 we conclude with selected application examples which demonstrate the feasibility and good performance of the method.

2 Thin-Shell with a Crack Through the Thickness

2.1 Kinematic description

We begin with a brief review of the assumed finite kinematics of the Kirchhoff-Love type shell model [5]. Subsequently, the extension of the kinematic description to the case of a fractured shell body is introduced. For alternative kinematic models for shells we refer to [2; 3; 28] and references therein.

Consider a shell body of uniform reference thickness $\overline{h}$ occupying a reference configuration $\overline{V}$, parametrized with convective coordinates θ^1, θ^2, and θ^3

$$\overline{\boldsymbol{\varphi}}(\theta^1,\theta^2,\theta^3) = \overline{\boldsymbol{x}}(\theta^1,\theta^2) + \theta^3 \overline{\boldsymbol{a}}_3(\theta^1,\theta^2) \quad \text{with} \quad -\frac{\overline{h}}{2} \leq \theta^3 \leq \frac{\overline{h}}{2}\,. \tag{2.1}$$

The position of the shell middle surface is given by $\overline{\boldsymbol{x}}$ and the unit normal to the middle surface also known as the shell director is defined by

$$\overline{\boldsymbol{a}}_3 = \frac{\overline{\boldsymbol{a}}_1 \times \overline{\boldsymbol{a}}_2}{|\overline{\boldsymbol{a}}_1 \times \overline{\boldsymbol{a}}_2|} \tag{2.2}$$

with the covariant surface basis vectors [1]

$$\overline{\boldsymbol{a}}_\alpha = \overline{\boldsymbol{x}}_{,\alpha} = \frac{\partial \overline{\boldsymbol{x}}}{\partial \theta^\alpha}\,.$$

The mapping $\boldsymbol{\varphi}$ maps the shell body into the deformed configuration V

$$\boldsymbol{\varphi}(\theta^1,\theta^2,\theta^3) = \boldsymbol{x}(\theta^1,\theta^2) + \theta^3 \lambda \boldsymbol{a}_3(\theta^1,\theta^2) \quad \text{with} \quad -\frac{\overline{h}}{2} \leq \theta^3 \leq \frac{\overline{h}}{2}\,. \tag{2.3}$$

[1] In the derivations the index notation is used where the Greek indices range from 1 to 2 and the Latin indices from 1 to 3. Further, a comma is used to denote partial differentiation and the summation convention is assumed to be in force.

The thickness stretch parameter $\lambda = h/\overline{h} > 0$ relates the deformed shell thickness h to the reference shell thickness $\overline{h}$. We use a Kirchhoff-Love type kinematic assumption and assume that the deformed director $\boldsymbol{a}_3$ is normal to the deformed shell middle surface

$$\boldsymbol{a}_3 = \frac{\boldsymbol{a}_1 \times \boldsymbol{a}_2}{|\boldsymbol{a}_1 \times \boldsymbol{a}_2|} \,. \tag{2.4}$$

With the previous assumptions the deformation gradient $\boldsymbol{F}$ of the deformation mapping $\boldsymbol{\varphi} \circ \overline{\boldsymbol{\varphi}}^{-1}$ can be written as

$$\boldsymbol{F} = \frac{\partial \boldsymbol{\varphi}}{\partial \overline{\boldsymbol{\varphi}}} = \frac{\partial \boldsymbol{\varphi}}{\partial \theta^i} \otimes \overline{\boldsymbol{g}}^i = \boldsymbol{a}_\alpha \otimes \overline{\boldsymbol{g}}^\alpha + \lambda \boldsymbol{a}_3 \otimes \overline{\boldsymbol{g}}^3 + \theta^3 (\lambda \boldsymbol{a}_3)_{,\alpha} \otimes \overline{\boldsymbol{g}}^\alpha \,, \tag{2.5}$$

where $\overline{\boldsymbol{g}}^i = \partial \theta^i / \partial \overline{\boldsymbol{\varphi}}$ are the contravariant basis vectors of the undeformed configuration.

Next, we assume the existence of a crack in the shell body with the two opposite crack flanks $\Gamma_C^+ \times [-h^+/2, h^+/2]$ and $\Gamma_C^- \times [-h^-/2, h^-/2]$ lying on the plus and minus sides of the crack, denoted by $+$ and $-$, respectively (see Fig. 2.1). The two curves Γ_C^+ and Γ_C^- on the middle surface have in the parameter space (θ^1, θ^2) the same parametric representation

$$\theta^1 = \theta^1(\xi) \quad , \quad \theta^2 = \theta^2(\xi) \quad \text{with} \quad \xi \in \mathbb{R} \,. \tag{2.6}$$

The deformation is generally discontinuous across the crack and has a jump

$$[\![\boldsymbol{\varphi}]\!] = \boldsymbol{\varphi}^+ - \boldsymbol{\varphi}^- \,. \tag{2.7}$$

Using the previous kinematic assumptions (2.3), the jump in the deformation can be written as

$$[\![\boldsymbol{\varphi}]\!] = [\![\boldsymbol{x}]\!] + \theta^3 [\![\lambda \boldsymbol{a}_3]\!] \,. \tag{2.8}$$

Note that the first term describes the discontinuity in the middle surface deformation and the second term the discontinuity in the shell normal. The discontinuities in the deformations can also be interpreted as the "opening displacement" of the crack.

For the subsequent derivations, we decompose the jump $[\![\boldsymbol{\varphi}]\!]$ into a normal and a shear component with respect to a local coordinate frame attached to the crack. To that purpose we first define an average unit normal $\boldsymbol{n}$ to the crack flanks $\Gamma_C^+ \times [-h^+/2, h^+/2]$ and $\Gamma_C^- \times [-h^-/2, h^-/2]$

$$\boldsymbol{n} = \frac{\frac{1}{2}(\boldsymbol{n}^+ + \boldsymbol{n}^-)}{|\frac{1}{2}(\boldsymbol{n}^+ + \boldsymbol{n}^-)|} \,. \tag{2.9}$$

The crack surface normal vectors $\boldsymbol{n}^\pm$ are computed from the tangent vectors $\boldsymbol{t}^\pm$ and the shell directors $\boldsymbol{a}_3^\pm$

$$\boldsymbol{n}^\pm = \boldsymbol{t}^\pm \times \boldsymbol{a}_3^\pm \,. \tag{2.10}$$

The tangent vectors are computed from the parametric location of the crack flanks (2.6) and the deformation mapping

$$\boldsymbol{t}^\pm = \frac{\partial \boldsymbol{\varphi}^\pm}{\partial \theta^\alpha} \frac{\partial \theta^\alpha}{\partial \xi} \,. \tag{2.11}$$

Thus, the jump in the deformations $[\![\boldsymbol{\varphi}]\!]$, here and henceforth denoted with $\boldsymbol{\delta}$, can be decomposed into the normal and tangential components δ_n and δ_s, given respectively by

$$\delta_n = \boldsymbol{\delta} \cdot \boldsymbol{n} \,, \qquad \boldsymbol{\delta}_s = \boldsymbol{\delta} - \delta_n \boldsymbol{n} = (\boldsymbol{I} - \boldsymbol{n} \otimes \boldsymbol{n}) \boldsymbol{\delta} \,, \qquad \delta_s = |\boldsymbol{\delta}_s| \,. \tag{2.12}$$

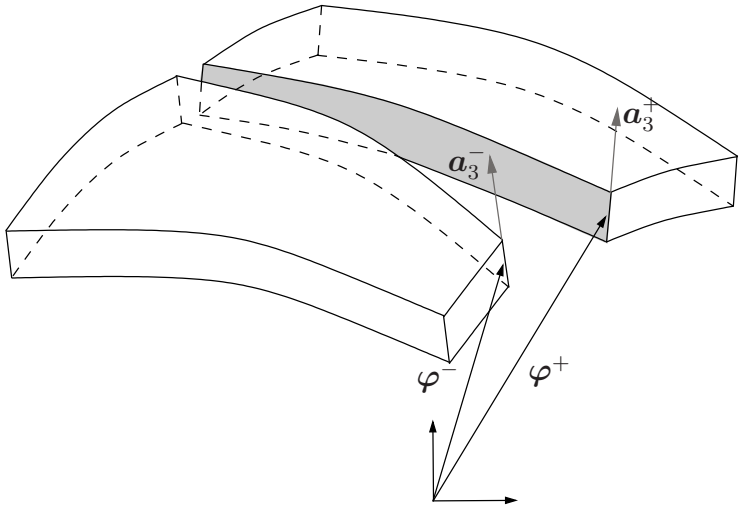

Figure 2.1: Fractured shell body: Opposite crack flanks and corresponding directors $\boldsymbol{a}_3$.

2.2 Weak form of the equilibrium

A standard semi-inverse approach is followed for deriving the shell equilibrium equations in weak form. The assumed reduced kinematic equations for the shell body (2.1 and 2.3) are introduced into the virtual work expression for the three-dimensional body

$$\delta\Pi_{\text{int}} - \delta\Pi_{\text{ext}} = 0 \tag{2.13}$$

with the internal and external virtual work $\delta\Pi_{\text{int}}$ and $\delta\Pi_{\text{ext}}$, respectively. In combination with proper boundary conditions, which have been omitted here for brevity, the weak form gives the equilibrium configurations of the shell body. As previously mentioned, we consider fracture as a gradual separation phenomenon, resisted by cohesive tractions. Consequently, the internal virtual work expression contains the virtual work of the cohesive interface in addition to the virtual work of the bulk material

$$\delta\Pi_{\text{int}} = \delta\Pi_{S,\text{int}} + \delta\Pi_{C,\text{int}} \tag{2.14}$$

with

$$\delta\Pi_{S,\text{int}} = \int_{\overline{\Omega}} \int_{-\overline{h}/2}^{\overline{h}/2} \boldsymbol{P} : \delta\boldsymbol{F}\, \mu\, d\theta^3 d\overline{\Omega} \tag{2.15a}$$

$$\delta\Pi_{C,\text{int}} = \int_{\overline{\Gamma}_C} \int_{-\overline{h}/2}^{\overline{h}/2} \boldsymbol{T} \cdot \delta\boldsymbol{\delta}\, \mu\, d\theta^3 d\overline{\Gamma}_C\,, \tag{2.15b}$$

where $\boldsymbol{P}$ is the first Piola-Kirchhoff stress tensor, $\boldsymbol{T}$ is the related traction vector at the cohesive surface, and μ accounts for the curvature of the shell in the computation of the volume [5]. Note that for hyperelastic constitutive models, with internal energy density W for the bulk material and ϕ for the cohesive interface, the tensor $\boldsymbol{P}$ and the vector $\boldsymbol{T}$ may be derived from

$$\boldsymbol{P} = \frac{\partial W}{\partial \boldsymbol{F}}\,, \qquad \boldsymbol{T} = \frac{\partial \phi}{\partial \boldsymbol{\delta}}\,. \tag{2.16}$$

Substituting the shell kinematics (2.5 and 2.8) into internal virtual work expression (2.15) gives

$$\begin{aligned}\delta\Pi_{\text{int}} &= \int_{\overline{\Omega}}\int_{-\overline{h}/2}^{\overline{h}/2} \boldsymbol{P} : \left(\delta\boldsymbol{a}_\alpha \otimes \overline{\boldsymbol{g}}^\alpha + \delta\boldsymbol{a}_3 \otimes \overline{\boldsymbol{g}}^3 + \theta^3\lambda\,\delta\boldsymbol{a}_{3,\alpha} \otimes \overline{\boldsymbol{g}}^\alpha\right)\, \mu\, d\theta^3 d\overline{\Omega} \\ &+ \int_{\overline{\Gamma}_C}\int_{-\overline{h}/2}^{\overline{h}/2} \boldsymbol{T} \cdot \left(\delta[\![\boldsymbol{x}]\!] + \theta^3\lambda\delta[\![\boldsymbol{a}_3]\!]\right)\, \mu\, d\theta^3 d\overline{\Gamma}_C\,. \end{aligned} \tag{2.17}$$

In (2.17) we disregard the spatial variation of the thickness stretch parameter λ. Following [5], the thickness stretch λ is computed from enforcing the thin-shell typical plane stress assumption on the constitutive level (see Section 4).
The stress resultant $\boldsymbol{n}^i$ and the coupled force $\boldsymbol{m}^\alpha$ for the shell are defined as

$$\boldsymbol{n}^i = \int_{-\overline{h}/2}^{\overline{h}/2} \boldsymbol{P}\boldsymbol{F}^T \cdot \boldsymbol{g}^i\, \mu\, d\theta^3\,, \qquad \boldsymbol{m}^\alpha = \int_{-\overline{h}/2}^{\overline{h}/2} \boldsymbol{P}\boldsymbol{F}^T \cdot \boldsymbol{g}^\alpha\, \theta^3\, \mu\, d\theta^3 \tag{2.18}$$

and substituting them into the internal work of the bulk material gives a more compact expression

$$\delta\Pi_{S,\text{int}} = \int_{\overline{\Omega}} \left[\boldsymbol{n}^\alpha \cdot \delta\boldsymbol{a}_\alpha + \boldsymbol{n}^3 \cdot \delta\boldsymbol{a}_3 + \boldsymbol{m}^\alpha\lambda\,\delta\boldsymbol{a}_{3,\alpha}\right]\, d\overline{\Omega}\,. \tag{2.19}$$

For dynamic problems, the weak form of equilibrium is augmented by the virtual kinetic work

$$\delta\Pi_{\text{kin}} + \delta\Pi_{\text{int}} - \delta\Pi_{\text{ext}} = 0 \tag{2.20}$$

with

$$\delta\Pi_{\text{kin}} = \int_{\overline{\Omega}}\int_{-\overline{h}/2}^{\overline{h}/2} \overline{\rho}\ddot{\boldsymbol{\varphi}} \cdot \delta\boldsymbol{\varphi}\, \mu\, d\theta^3 d\overline{\Omega}\,, \tag{2.21}$$

where $\overline{\rho}$ is the initial mass density of the bulk material and $\ddot{\boldsymbol{\varphi}}$ is the acceleration vector.

3 Subdivision Thin-Shell Elements

The reference ($\overline{\boldsymbol{x}}$) and deformed ($\boldsymbol{x}$) shell middle surfaces are discretized with smooth subdivision shape functions, as introduced in [6]. The interpolation within one element is accomplished with shape functions which have support on the element as well as on the one-ring of neighboring elements (see Fig. 3.1)

$$\overline{\boldsymbol{x}} = \sum_{I=1}^{NP} N^I \overline{\boldsymbol{x}}_I\,, \qquad \boldsymbol{x} = \sum_{I=1}^{NP} N^I \boldsymbol{x}_I\,. \tag{3.1}$$

The number of the control points NP involved in the interpolation of each element depends on the local connectivity of the mesh. For example, for regular patches where each of the three element vertices are incident to six elements the interpolant derived from the Loop's subdivision scheme has $NP = 12$ control points [16; 31]. The overlapping local interpolations, each over one patch, combined lead to a global interpolation with square integrable curvatures.

In presence of fracture, the smoothness and/or continuity of the interpolation has to be relaxed. In our implementation, we assume that cracks can only nucleate and propagate along element

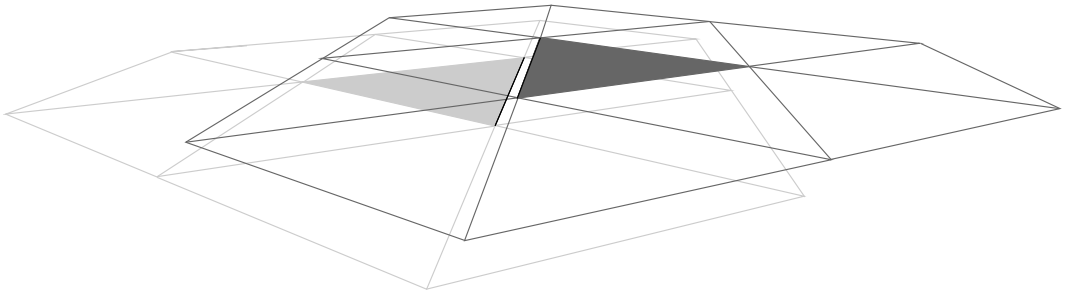

Figure 3.1: One cohesive edge and the two elements with their one neighborhoods.

Figure 3.2: Support for the subdivision interpolation over one (dark) edge, i.e., only the shown vertices contribute to the interpolation over the dark edge.

edges. Furthermore, once fracture nucleates, the element patches on the left and right side of the cracked edge interact only through cohesive tractions. The cohesive tractions are self-balanced internal forces derived from a cohesive fracture model (see Section 4.2). The topological changes necessary to the non-local subdivision functions and the underlying control mesh in order to describe the propagation of a single crack are rather complicated. Therefore, we chose to pre-fracture all the element patches, so that each patch possesses its own nodes and acts independently for the purpose of interpolation. Each element patch consists of a triangular element and all the nodes in the one neighborhood of that element (see Fig. 3.1). The resulting interpolation of the shell middle surface is always smooth over one triangle and allows discontinuities along the edges depending on the positioning of the control nodes. Prior to crack nucleation, we propose two alternative approaches to enforce the coupling between the distinct elements. In the first approach the interaction of the elements is enforced by a stiff elastic cohesive interface model applied at all non cracked edges. Once a crack nucleates, the interface model on that edge is replaced with a conventional cohesive model (see Section 4.2). In the second approach, all the vertices which have the same coordinates in the reference configuration are initially algorithmically forced to have the same displacements. In the explicit dynamic case the related algorithmic procedures can easily be implemented with a pointer based data structure provided by, e.g., C/C++. Once a crack nucleates along an edge, all the vertices in the domain of influence of that edge are allowed to move independently (see Fig. 3.2). Furthermore, on all the edges connected to the two vertices of the cracked edge a cohesive interface is activated.

The discretization of the cohesive internal virtual work (2.17) with the subdivision shape func-

tions gives

$$\begin{aligned}\delta\Pi_{C,\text{int}} &= \int_{\overline{\Gamma}_C}\int_{-\overline{h}/2}^{\overline{h}/2}\Big\{\boldsymbol{T}\cdot\Big[\delta\Big(\sum N^I\boldsymbol{x}_I^+\Big)-\delta\Big(\sum N^I\boldsymbol{x}_I^-\Big)\Big]\\ &+ \theta^3\,\boldsymbol{T}\cdot\Big[\lambda^+\,\delta\boldsymbol{a}_3\Big(\sum N^I\boldsymbol{x}_I^+\Big)-\lambda^-\,\delta\boldsymbol{a}_3\Big(\sum N^I\boldsymbol{x}_I^-\Big)\Big]\Big\}\,\mu\,d\theta^3 d\overline{\Gamma}_C\,. \qquad (3.2)\end{aligned}$$

Thus, the internal forces at the vertex I are given by

$$\boldsymbol{f}_{\text{int}}^{I\pm}=\frac{\partial\Pi_{int}}{\partial\boldsymbol{x}_I^\pm}=\pm\int_{\overline{\Gamma}_C}\int_{-\overline{h}/2}^{\overline{h}/2}\boldsymbol{T}N^I\,\mu\,d\theta^3 d\overline{\Gamma}_C\pm\int_{\overline{\Gamma}_C}\int_{-\overline{h}/2}^{\overline{h}/2}\theta^3\,\lambda^\pm\,\boldsymbol{T}\cdot\frac{\partial\boldsymbol{a}_3(\sum N^J\boldsymbol{x}_J^\pm)}{\partial\boldsymbol{x}_I^\pm}\,\mu\,d\theta^3 d\overline{\Gamma}_C\,. \qquad (3.3)$$

The integral over the cohesive surface is numerically integrated with different rules along the edge $\overline{\Gamma}_C$ and across the thickness $[-\frac{\overline{h}}{2},\frac{\overline{h}}{2}]$. Along the edge we use three Gauss points and across the thickness more than three Simpson points. The integrals over the shell middle surface $\overline{\Omega}$ are numerically integrated with seven Gauss points, which is exact for up to fifth order polynomials [36]. The contribution of the shell to the internal force vector is equivalent to the non-fractured shell (see [5] for details).

4 Constitutive Models

In the previous work on subdivision shells [5; 6; 7] compressible as well as incompressible hyperelastic material models have been used. In the present extension, we assume a viscoplastic behavior for the bulk and a cohesive model to account for the crack propagation.

4.1 Finite deformation viscoplasticity

The inelastic behavior of the shell is described with a rate dependent finite deformation viscoplasticity model, based on a standard multiplicative decomposition of the deformation gradient into an elastic and inelastic part. We apply the fully implicit method proposed by Cuitiño and Ortiz in [9], where, by using logarithmic and exponential mappings, the constitutive update algorithms used for small strain plasticity are extended to finite plasticity.

The small strain plasticity model is a conventional J_2 model with isotropic power-law hardening and power-law viscosity. The power-law hardening for the flow stress g has the form

$$g(\epsilon^p)=\sigma_y\left(1+\frac{\epsilon^p}{\epsilon_0^p}\right)^{1/n}, \qquad (4.1)$$

where σ_y is the initial yield stress, ϵ^p and ϵ_0^p are the total and the reference plastic strains, respectively, and $1/n$ is the hardening exponent. The rate-dependent behavior is described in terms of the effective von Mises stress σ_{eff} with a power viscosity law and constant rate sensitivity

$$\sigma_{\text{eff}}=g(\epsilon^p)\left(1+\frac{\dot{\epsilon}^p}{\dot{\epsilon}_0^p}\right)^{1/m}, \qquad (4.2)$$

where $\dot{\epsilon}_0^p$ is the reference plastic strain rate and $1/m$ the strain rate sensitivity exponent.

Effectively, the constitutive update algorithm gives the first Piola-Kirchhoff tensor $\boldsymbol{P}$ for a given deformation gradient $\boldsymbol{F}$ and a set of history dependent variables. The equivalent Kirchhoff stress tensor $\boldsymbol{\tau} = \boldsymbol{P}\boldsymbol{F}^T$ and its components in the deformed covariant basis $\boldsymbol{\tau} = \tau^{ij}\, \boldsymbol{g}_i \otimes \boldsymbol{g}_j$, with $\boldsymbol{g}_i = \partial\boldsymbol{\varphi}/\partial\theta_i$, can be computed by applying proper transformations. The value of the thickness stretch parameter λ is computed iteratively, e. g., by means of a Newton-Raphson iteration, from the plane stress condition $\tau^{33} = 0$ (see, e. g., [5; 10] for details).

4.2 Cohesive interface model

In the computations subsequently presented we employ an irreversible cohesive model of the general form proposed in [19]. In this model, the opening displacement $\boldsymbol{\delta}$ plays the role of a deformation measure while the tractions $\boldsymbol{T}$ is the conjugate stress measure. The free energy density per unit undeformed area is assumed to be of the form

$$\phi = \phi(\delta, \boldsymbol{q}) \,, \tag{4.3}$$

where $\boldsymbol{q}$ is a suitable set of internal variables and δ is a scalar effective opening displacement

$$\delta = \sqrt{\beta^2\delta_S^2 + \delta_n^2} \tag{4.4}$$

defined in terms of the normal δ_n and sliding δ_s opening displacements, as defined in (2.12). The parameter β effectively assigns different weights to the sliding and opening displacements. It can be shown, [19], that the relation between the opening displacement and cohesive traction is of the form

$$\boldsymbol{T} = \frac{T}{\delta}(\beta^2\boldsymbol{\delta}_S + \delta_n\boldsymbol{n}) \tag{4.5}$$

with the scalar effective traction

$$T = \frac{\partial\phi}{\partial\delta}(\delta, \boldsymbol{q}) \,. \tag{4.6}$$

Equation (4.5) identifies β as the ratio between the shear and the normal cohesive strength of the material. The parameter β can alternatively be regarded as the ratio of mode II to mode I fracture toughness of the bulk material [19]. In the calculations we employ the monotonic envelope shown in Fig. 4.1, and unloading is assumed to occur towards the origin. The parameters of the model are the maximum tensile stress σ_c and the mode I fracture energy density G_c. The critical opening displacement is then given by $\delta_c = 2G_c/\sigma_c$.

As noted in the foregoing, we sidestep the need to track the topological transitions due to the insertion of cohesive elements by pre-fracturing all shell-element edges. In explicit dynamic calculations, conformity at the edges prior to crack nucleation can , e.g., be enforced by a projection method consisting of nodal momentum averaging. In the subsequently presented computations conformity is enforced by a penalty method. This effectively amounts to replacing the initial rigid portion of the cohesive law by a stiff linear response of the form

$$\boldsymbol{T} = k\boldsymbol{\delta} \,, \tag{4.7}$$

where k is a penalty parameter. In tension, this relation is replaced by the proper cohesive law when $k\delta$ reaches σ_c. Under compression the penalty relation serves the purpose of enforcing the closure constraint. In particular, in bending dominated fracture, part of the shell thickness may be under compression, and hence uncracked, whereas the remainder of the thickness may be opening as a part-through crack.

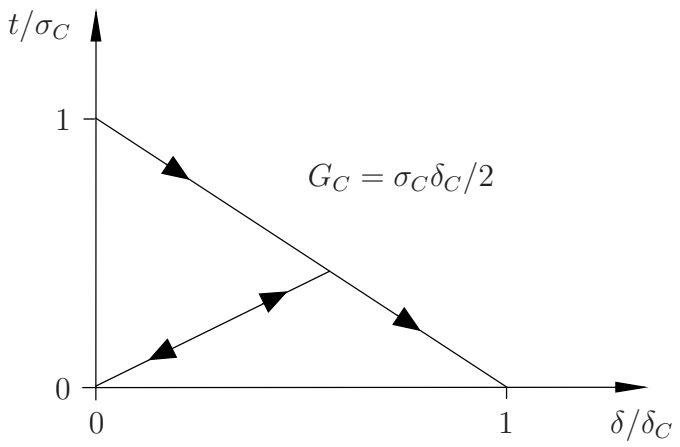

Figure 4.1: Linearly decreasing monotonic envelop with loading and unloading [21].

5 Applications

5.1 Square plate

In order to gain insight into the sensitivity of the numerical solution on the choice of the penalty parameter k (4.7) we consider a simply supported plate with a pre-fractured shell model. The plate is linear elastic and the penalty relation (4.7) is used in lieu of a cohesive law. This reduced model is similar in spirit to the interior penalty method for the bilaplacian equation introduced by Babuska et al. [1]. It is known that this method has an inherent consistency error and therefore the convergence in the energy norm is not optimal. However, optimal convergence can be attained by means of a correction proposed by Hansbo et al. [11].

The simply supported square plate has an edge length $L = 1$ and a thickness $h = 0.1$ and is subjected to uniform static pressure loading of $p = 0.1$. We choose a Young's modulus $E = 69000$ and a Poisson's ratio $\nu = 0.3$. The plate is discretized into 1024 elements and the deflected shapes are computed for $k/E = 500$, 1000, 5000, 10000, and 50000. Fig. 5.1 shows the normalized maximum out of plane displacement as function of the penalty coefficient k. The displacements are normalized with the analytical series solution of $6.425 \cdot 10^{-5}$ [29]. It follows from this analysis that the non-fractured solution is ostensibly recovered for modestly large values of k.

5.2 Petalling of aluminum plates

The present framework can be applied to a variety of thin plate and shell fracture and fragmentation problems, such as the perforation of thin-plates impacted by fast moving projectiles [8; 13; 14; 26; 27; 34].

As an example of application, we simulate the experiments of Landkof and Goldsmith [14] concerned with the petalling failure of circular aluminum plates with and without initial holes struck by hard-steel conical projectiles. In the experiments of Landkof and Goldsmith under consideration, the circular aluminum (Al2024-0) target plates have a diameter of 139.7 mm and a thickness of 1.27 mm or 3.175 mm. For the plates with an initial hole at the center of the plate, the hole

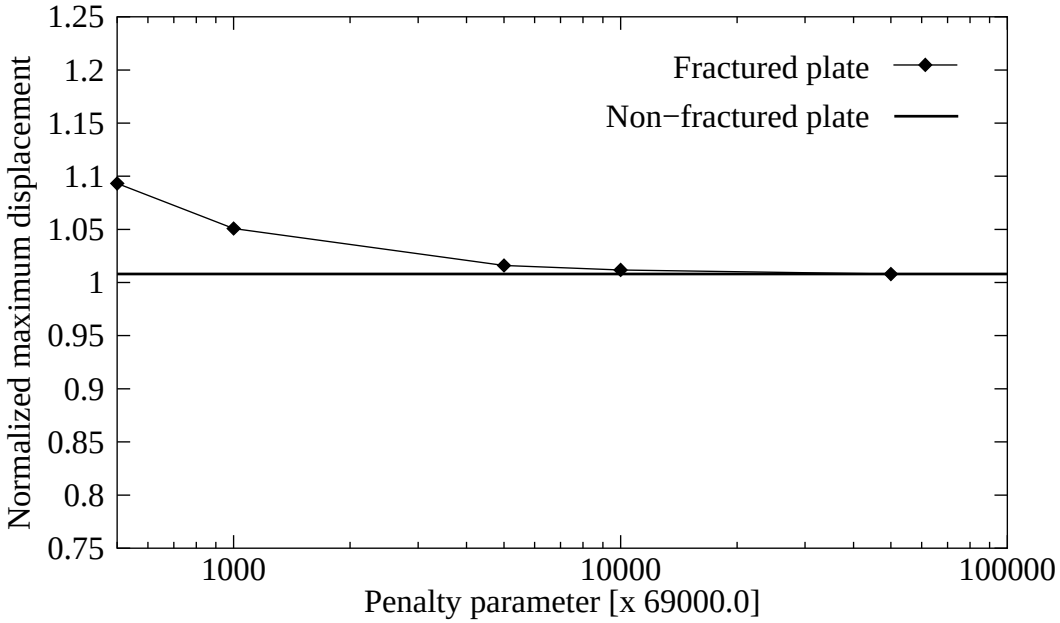

Figure 5.1: Sensitivity on the penalty coefficient k, eq. (4.7): maximum out of plane displacement of a pre-fractured simply supported square plate under uniform pressure.

diameter is 4.76 mm, 6.35 mm, or 9.53 mm. The heat-treated steel projectile is cylindrical-conical in shape and has a diameter of $d_b = 12.7$ mm, a length of $L_b = 35.55$ mm, and a weight of $m_b = 29.5$ g. The projectile has a striking velocity in the range of 300-600 m/s. The projectile velocity after passing through the target plate was measured and compared with the predictions of analytical models based on energetic considerations [14]. In calculations we consider a solid plate and a perforated plate with a 6.35 mm diameter hole. The plate thickness is 3.175 mm in both cases. The striking velocity is $v_i = 320$ m/s. The bulk material response of the aluminum plates is assumed to obey the J2-plasticity model described in section (4.1). The material parameters for the plasticity model are provided in [14] and are collected in Table 1. The material properties chosen for the cohesive model are collected in Table 2. The weighting coefficient β has been chosen according to previous computations on aluminum specimens [21]. The finite element meshes used

Mass density	$\rho = 2719$ kg/m^3
Young's modulus	$E = 69000$ MPa
Poisson's ratio	$\nu = 0.33$
Yield stress	$\sigma_0 = 90$ MPa
Reference plastic strain	$\varepsilon_0^p = 0.001$
Hardening exponent	$1/n = 4$
Reference plastic strain rate	$\dot{\varepsilon}_0^p = 0.0001$ 1/s
Rate sensitivity exponent	$1/m = 0.01$

Table 1: J2-plasticity model with power-law hardening and rate dependency: material properties for the bulk behavior of Al2024-0 [14].

Cohesive strength	$\sigma_c = 180$ MPa
Fracture energy	$G_c = 2.75$ N/m
Weighting coefficient	$\beta^2 = 0.75$
Penalty parameter	$k = 100E$

Table 2: Linearly decreasing irreversible cohesive model: material properties and the algorithmic parameter k used for the fractured interfaces.

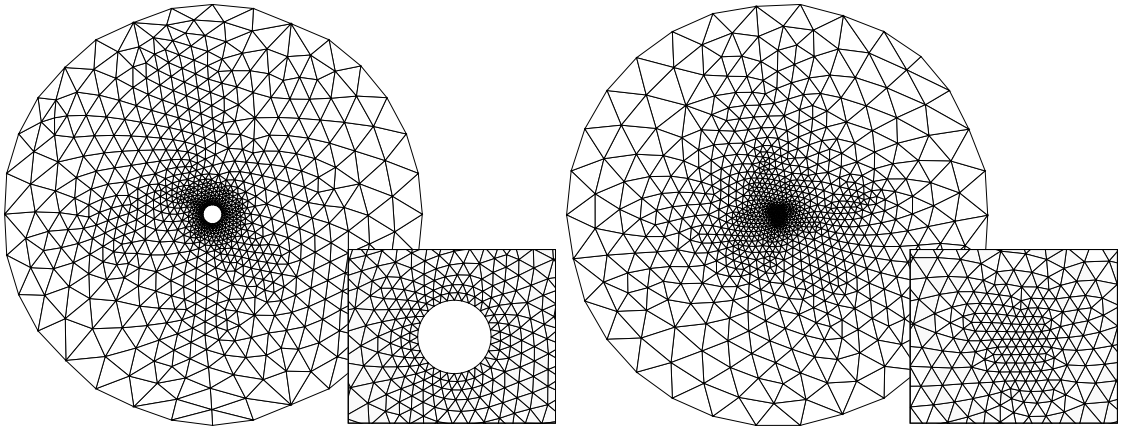

(a) (b)

Figure 5.2: Finite element meshes with detail of the central part. (a) Plate with a $6.25mm$ hole: 820 nodes, 1576 subdivision shell elements; (b) Intact plate: 886 nodes and 1740 subdivision shell elements.

in calculations are shown in Fig. 5.2. The time step of 0.00045 μs is chosen to be smaller than the critical time step for explicit integration. To contain the numerical effort, we decided not to model the contact between the plate and projectile. The effect of the projectile impact is simply simulated by applying a pressure history over the impact area corresponding to the force exerted by the conical tip of the projectile. The impact force has been computed from the deceleration Δv of the projectile, as measured in the experiments [14]. We begin by estimating the time for the projectile to cross the plate with as the ratio between the projectile length and initial bullet velocity, with the result

$$\Delta t = \frac{L_b}{v_b} \,. \tag{5.1}$$

A rough estimate of the impact force F is thus given by the deceleration times the bullet mass

$$F = m_b \, \frac{\Delta v}{\Delta t} \,. \tag{5.2}$$

The average impact pressure corresponding to the force F is computed as

$$p_i = \frac{F}{A_i} = \frac{4\,F}{\pi\, d_b^2} \,, \qquad p_h = \frac{F}{A_i} = \frac{4\,F}{\pi\,(d_b^2 - d_h^2)} \,, \tag{5.3}$$

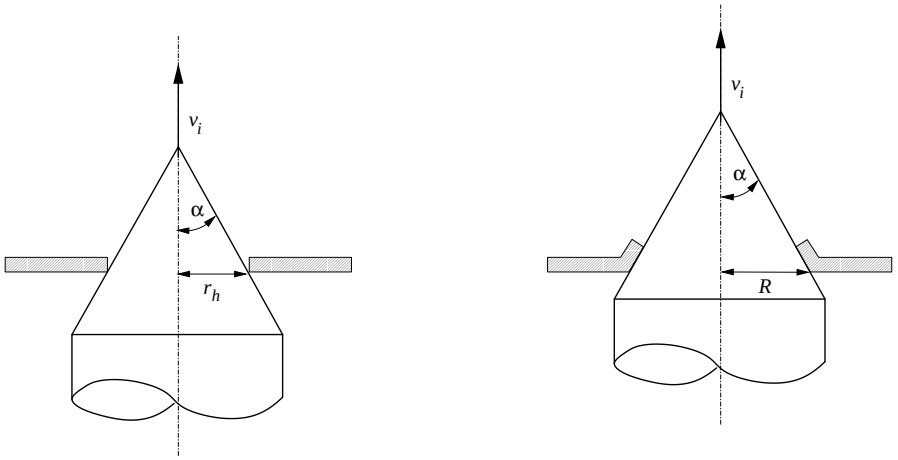

Figure 5.3: Motion of the projectile and progressive enlargement of the contact area.

where p_i refers to the solid plate and p_h to the plate with a hole. Based on an average velocity drop $\Delta v = 40$ m/s, in simulations we set $p_i = 159$ N/mm^2 and $p_h = 213$ N/mm^2. In order to account for the conical shape of the projectile nose, the pressure (see Fig. 5.3) is applied on a progressively increasing circular area of radius

$$R = \frac{d_h}{2} + \frac{v_i}{\tan\alpha}\, t \leq \frac{d_b}{2}\,, \tag{5.4}$$

where $\alpha = 30^\circ$ is the half-cone angle of the projectile tip, and t the time from impact. The initial radius $R|_{t=0} = d_h/2$ is zero for solid plates.

The results of the dynamical analysis of the perforated plate are collected in Fig. 5.4. As may be seen in the figure, the calculations reveal the consecutive stages of the perforation of the plate. In keeping with theory and experiment [14], the early states of penetration are characterized by an enlargement of the hole, Fig. 5.4a, followed by crack propagation, Fig. 5.4b, and final bending of trapezoidal petals, Fig. 5.4c. A detail of the central part of the plate at the end of the calculation is shown in Figure 5.5. It is interesting to note in Figure 5.5a how a dominant crack forms which effectively shuts off numerous other smaller cracks. Eventually, the dominant crack branches and arrests, and several other cracks propagate in its place, Figure 5.5b. Of course, the fine details of the fracture patterns are to some extend stochastic and are likely to exhibit considerable scatter. For present purposes it suffices to point out that the numerical method allows for complex fracture patterns including branching and fragmentation. As observed in [14], for solid plates petalling starts with the formation of a star-shaped crack at the impact point, and the subsequent propagation of radial cracks. The resulting triangular petals rotate about a continuously shifting circular plastic hinge in order to allow the passage of the projectile. The different stages of penetration can be clearly seen in Fig. 5.6. A detail of the central part of the plate after the formation of the star shaped crack is shown in Fig. 5.7. The branching events in some of the radial cracks are particularly noteworthy.

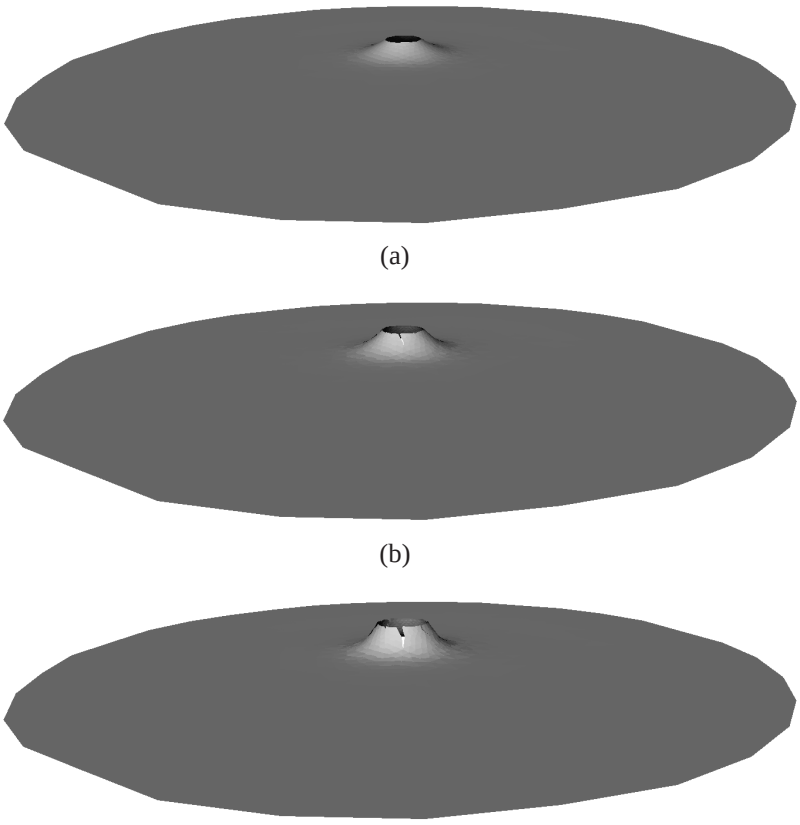

(a)

(b)

(c)

Figure 5.4: Perforated plate, projectile perforation history: a) Enlargement of the hole; b) crack propagation; and c) bending of trapezoidal petals.

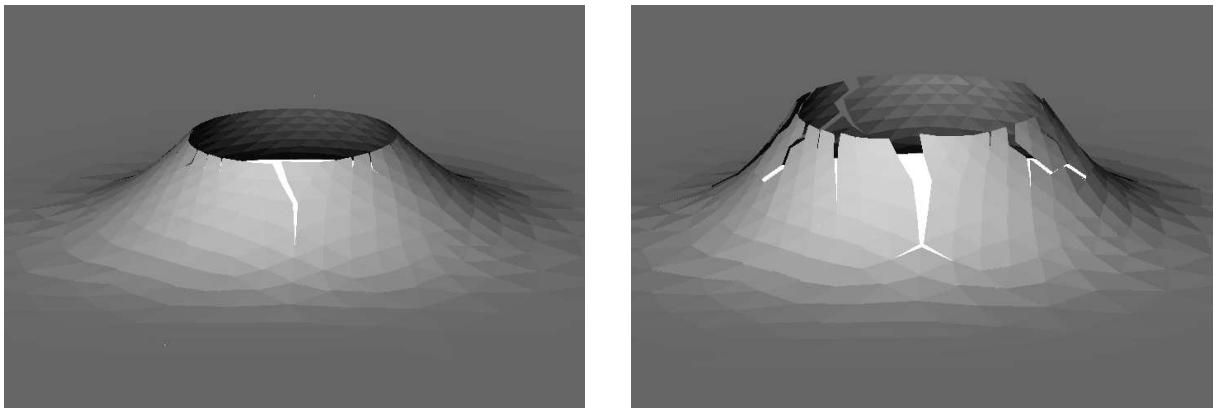

(a) (b)

Figure 5.5: Perforated plate: a) Detail of the petalling pattern; b) final configuration.

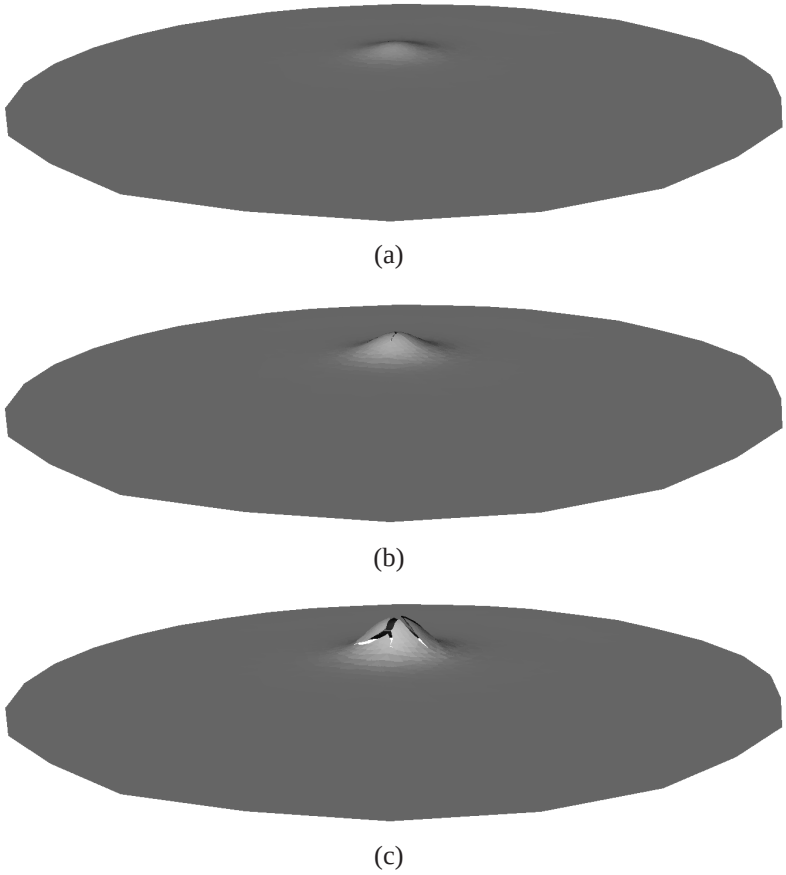

(a)

(b)

(c)

Figure 5.6: Solid plate, projectile perforation history: a) Initial radial cracking; b) crack propagation; and c) bending of triangular petals.

6 Summary and Concluding Remarks

We have presented a thin-shell subdivision finite-element method augmented with cohesive fracture and fragmentation capabilities. The present approach is based on the simple device of prefracturing all shell-element edges. Thus, in contrast to the original subdivision-element discretization introduced in [6], each element patch possesses its own full complement of nodes. Initially the elements are forced to be conforming by means of constraints, which later also serve the purpose of enforcing closure. The constraints are active on an edge until an effective traction attains a prescribed threshold. Subsequently, the interaction of the two elements incident on a edge is mediated by a cohesive element encoding a cohesive law. The cohesive model accounts for in-plane or tearing, shearing, and bending of hinge modes of fracture.

The versatility and good performance of the method has been demonstrated with selected examples of petalling in thin aluminum plates. In particular, we have simulated the experiments of Landkof and Goldsmith [14], which concern the penetration of a circular plate with or without an initial perforation by a steel projectile of conical tip. The simulations showcase the ability of the method to track the formation of complex fracture patterns, possibly involving branching and fragmentation.

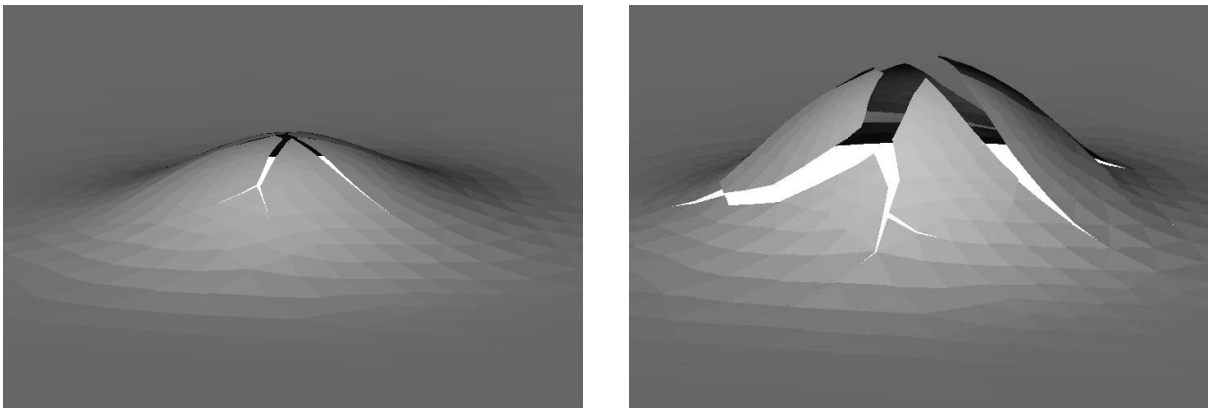

(a) (b)

Figure 5.7: Solid plate: a) Star-shaped crack formation; b) final configuration.

In closing, we note some of the limitations of the method. Thus, the pre-fracture of all edges results in a substantial increase in the number of degrees of freedom of the model, and therefore adds to the computational expense. The introduction of penalty parameters may result in stiff systems and the need for careful preconditioning. Clearly, an adaptive implementation based on the insertion of cohesive elements would be much preferable, but a comprehensive classification of the topological transitions attendant to element insertion, and a set of rules for updating the mesh representation accordingly, are beyond our grasp at this time and are left for future research.

Acknowledgements The support of DoE through Caltech's ASCI Center for the Simulation of the Dynamic Response of Materials (DOE W-7405-ENG-48, B523297) is gratefully acknowledged. MO is also grateful for partial support from the Office of Naval Research through grant N00014-96-1-0068.

References

[1] I. Babuska and Zlamal M. Nonconforming elements in the finite element method with penalty. *Siam Journal on Numerical Analysis*, 10(5):863–875, 1973.

[2] N. Büchter and E. Ramm. Shell theory versus degeneration - a comparison in large rotation finite element analysis. *International Journal for Numerical Methods in Engineering*, 34:39–59, 1992.

[3] N. Buchter, E. Ramm, and D. Roehl. 3-dimensional extension of nonlinear shell formulation based on the enhanced assumed strain concept. *International Journal for Numerical Methods in Engineering*, 37:2551–2568, 1994.

[4] G. T. Camacho and M. Ortiz. Computational modelling of impact damage in brittle materials. *International Journal of Solids and Structures*, 33(20–22):2899–2938, 1996.

[5] F. Cirak and M. Ortiz. Fully c^1-conforming subdivision elements for finite deformation thin-shell analysis. *International Journal for Numerical Methods in Engineering*, 51:813–833, 2001.

[6] F. Cirak, M. Ortiz, and P. Schröder. Subdivision surfaces: A new paradigm for thin-shell finite-element analysis. *International Journal for Numerical Methods in Engineering*, 47(12):2039–2072, 2000.

[7] F. Cirak, M.J. Scott, E.K. Antonsson, M. Ortiz, and P. Schröder. Integrated modeling, finite-element analysis, and engineering design for thin-shell structure using subdivision. *Computer Aided Design*, 34:137–148, 2002.

[8] P. E. Cros, L. Rota, C. E. Cottenot, R. Schirrer, and C. Fond. Experimental and numerical analysis of the impact behaviour of polycarbonate and polyurethane multilayer. *Journal de Physique IV*, 10(P9):671–676, 2000.

[9] A. Cuitino and M. Ortiz. A material-independent method for extending stress update algorithms from small-strain plasticity to finite plasticity with multiplicative kinematics. *Engineering Computations*, 9:437–451, 1992.

[10] R. de Borst. The zero-normal-stress condition in plane-stress and shell elastoplasticity. *International Journal for Numerical Methods in Engineering*, 7:29–33, 1991.

[11] A. Hansbo and M. G. Larson. A discontinuous galerkin method for the plate equation. *Calcolo*, 39:41–59, 2002.

[12] Hibbitt, Karlsson&Sorrensen, Pawtucket,RI. *Abaqus Theory Manual*, 2002.

[13] D. I. Hyun, S. M. Oak, S. S. Kang, and Y. H. Moon. Estimation of hole flangeability for high strength steel plates. *Journal of Materials Processing Technology*, 130(SI):9–13, 2002.

[14] B. Landkof and W. Goldsmith. Petalling of thin, metallic plates during penetration by cylindro-conical projectiles. *International Journal of Solids and Structures*, 21(3):245–266, 1985.

[15] H. Lee and D. M. Parks. Line-spring finite element for fully plastic crack growth - ii. surface cracked plate and pipes. *International Journal of Solids and Structures*, 35(36):5139–5158, 1998.

[16] C. Loop. Smooth subdivision surfaces based on triangles. Master's thesis, Departement of Mathematics, University of Utah, 1987.

[17] A. Needleman. A continuum model for void nucleation by inclusion debonding. *Journal of Applied Mechanics*, 54:525–531, 1987.

[18] A. Needleman. An analysis of decohesion along an imperfect interface. *International Journal of Fracture*, 42:21–40, 1990.

[19] M. Ortiz and A. Pandolfi. A class of cohesive elements for the simulation of three-dimensional crack propagation. *International Journal for Numerical Methods in Engineering*, 44:1267–1282, 1999.

[20] M. Ortiz and S. Suresh. Statistical properties of residual stresses and intergranular fracture in ceramic materials. *Journal of Applied Mechanics*, 60:77–84, 1993.

[21] A. Pandolfi, P. Krysl, and M. Ortiz. Finite element simulation of ring expansion and fragmentation: The capturing of length and time scales through cohesive models of fracture. *International Journal of Fracture*, 95:279–297, 1999.

[22] A. Pandolfi and M. Ortiz. Solid modeling aspects of three-dimensional fragmentation. *Engineering with Computers*, 14(4):287–308, 1998.

[23] A. Pandolfi and M. Ortiz. An efficient adaptive procedure for three-dimensional fragmentation simulations. *Engineering with Computers*, 18(2):148–159, 2002.

[24] D.M. Parks and White C.S. Elastic-plastic line-spring finite elements for surface-cracked plates and shells. *Journal of Pressure Vessel Technology*, 104(4):287–292, 1982.

[25] J.R. Rice and Levy N. The part-through surface crack in an elastic plate. *Journal of Applied Mechanics*, 39(1):185–194, 1972.

[26] W. Q. Shen. A study on the failure of circular plates struck by masses. part 2: theoretical analysis for the onset of failure. *International Journal of Impact Engineering*, 27(4):413–432, 2002.

[27] W. Q. Shen, N. O. Rieve, and B. Baharun. A study on the failure of circular plates struck by masses. part 1: experimental results. *International Journal of Impact Engineering*, 27(4):399–412, 2002.

[28] J.C. Simo and D.D. Fox. On a stress resultant geometrically exact shell model. part i: Formulation and optimal parameterization. *Computer Methods in Applied Mechanics and Engineering*, 72:267–304, 1989.

[29] S. Timoshenko and S. Woinowsky-Krieger. *Theory of Plates and Shells*. McGraw-Hill, 1959.

[30] V. Tvergaard and J. W. Hutchinson. Effect of strain dependent cohesive zone model on predictions of crack growth resistance. *International Journal of Solids and Structures*, 33:3297–3308, 1996.

[31] J. Warren and H. Weimer. *Subdivision Methods for Geometric Design: A Constructive Approach*. Academic Press, 2002.

[32] T. Wierzbicki. Petalling of plates under explosive and impact loading. *International Journal of Impact Engineering*, 22(9-10):935–954, 1999.

[33] T. Wierzbicki and G. N. Nurick. Large deformation of thin plates under localised impulsive loading. *International Journal of Impact Engineering*, 18(7-8):899–918, 1996.

[34] S. C. Wright, N. A. Fleck, and W. J Stronge. Ballistic impact of polycarbonate - an experimental investigation. *International Journal of Impact Engineering*, 13(1):1–20, 1993.

[35] X.-P. Xu and A. Needleman. Numerical simulations of fast crack growth in brittle solids. *Journal of the Mechanics and Physics of Solids*, 42(9):1397–1434, 1994.

[36] O.C. Zienkiewicz and R.L. Taylor. *The Finite Element Method*, volume 1. McGraw-Hill, 1989.